Benchtop Magnetic Shielding for Benchmarking Atomic Magnetometers

Peter J. Hobson, Niall Holmes, Prashant Patel, Ben Styles, James Chalmers, Chris Morley, Alister Davis, Michael Packer, Thomas X. Smith, Sintija Raudonyte, Darragh Holmes, Robert Harrison, David Woolger, Dominic Sims, Matthew J. Brookes, Richard Bowtell, and Mark Fromhold

***Abstract*— Here, a benchtop hybrid magnetic shield containing four mumetal cylinders and nine internal flexible printed circuit boards (flex-PCBs) is designed, constructed, tested, and operated. The shield is designed specifically as a test-bed for building and operating ultrasensitive quantum magnetometers. The geometry and spacing of the mumetal cylinders are optimized to maximize shielding efficiency while maintaining Johnson noise <15 fT/$\sqrt{\text{Hz}}$. Experimental measurements at the shield's center show passive shielding efficiency of $(1.0 \pm 0.1) \times 10^6$ for a 0.2-Hz oscillating field applied along the shield's axis. The nine flex-PCBs generate three uniform fields, which all deviate from perfect uniformity by ≤0.5% along 50% of the inner shield axis, and five linear field gradients and one second-order gradient, which all deviate by ≤4% from perfect linearity and curvature, respectively, over measured target regions. Together, the target field amplitudes are adjusted to minimize the remnant static field along 40% of the inner shield axis, as mapped using an atomic magnetometer. In this region, the active null reduces the norm of the magnitudes of the three uniform fields and six gradients by factors of 19.5 and 19.8, respectively, thereby reducing the total static field from 1.68 to 0.23 nT.**

***Index Terms*— Analytical models, coils, demagnetization, electromagnetic measurements, flexible printed circuits, Fourier transforms, magnetic shielding, magnetometers.**

I. Introduction

AN EXCEPTIONALLY low and controlled magnetic field is required to reduce noise in fundamental physics experiments [1], [2] and to benchmark ultrasensitive quantum magnetometers, including those based on NV-centers [3] and atomic vapors [4], [5], [6]. In particular, zero-field optically pumped magnetometers (OPMs) [7], [8] have diverse applications from functional neuroimaging [9], [10] to rapid diagnostics of electric batteries [11], [12], but require low static (no time variation) fields to reduce projection errors [13] and nonlinearities in sensor gain.

External magnetic fields may be attenuated by enclosing a region with passive shielding material. For low-frequency shielding, high permeability materials, such as *mumetal*, are used to divert magnetic flux. However, high permeability materials magnetize under applied fields, thereby limiting the shielding effect. Although this is mitigated by degaussing [14], [15], [16], some remnant magnetization usually remains. Coil systems inside passive shields are used to null offsets induced by magnetization and cancel leakage fields. These coils may be designed to account for the electromagnetic distortion induced by their coupling to passive shielding [17], [18], [19], [20], [21].

This article presents the design, construction, testing, and operation of a magnetic shield comprising nested mumetal cylinders with end caps and internal active coils. The nested cylinders are of a high permeability and their geometries and spacings are optimized to maximize their shielding effectiveness and minimize the weight of the shield, while ensuring that there is a large internal usable volume for experimentation. Entry hole positions are selected to maximize access to this useable volume without significantly diminishing the effectiveness of the passive shielding. The passive shielding performance is experimentally validated before nine active coils are constructed, housed on nested flexible printed circuit boards (flex-PCBs), within the inner mumetal shield. These coils are designed to null static offsets due to magnetization and residual external magnetic fields which pass through the passive shielding. The coupling of the active and passive components is included a priori in the design process to enhance the nulling process. The flex-PCBs are characterized in situ to validate the design procedure. Finally, the coil currents applied to the flex-PCBs are tuned to null the residual field along the inner shield's axis as measured using a zero-field OPM.

II. Passive Shielding

The passive shielding is constructed from four benchtop-sized nested co-axial and co-centered mumetal

Manuscript received 13 April 2023; accepted 21 June 2023. Date of publication 10 July 2023; date of current version 20 July 2023. This work was supported in part by U.K., Quantum Technology Hub Sensors and Timing under Grant EP/T001046/1; in part by the Innovate U.K., and the Engineering Research Council of Canada via Project through the Diamond NV Sensors for Quantum-Limited Magnetic Field Measurements; and in part by the Defense Science and Technology Laboratory. The Associate Editor coordinating the review process was Dr. Seyed Hossein Hesamedin Sadeghi. *(Corresponding author: Peter J. Hobson.)*

Peter J. Hobson, Chris Morley, Alister Davis, Michael Packer, Thomas X. Smith, Dominic Sims, and Mark Fromhold are with the School of Physics and Astronomy, University of Nottingham, NG7 2RD Nottingham, U.K. (e-mail: peter.hobson@nottingham.ac.uk).

Niall Holmes, Matthew J. Brookes, and Richard Bowtell are with the School of Physics and Astronomy, University of Nottingham, NG7 2RD, Nottingham, U.K., and also with the Sir Peter Mansfield Imaging Centre, University of Nottingham, NG7 2RD Nottingham, U.K.

Prashant Patel, Ben Styles, James Chalmers, Sintija Raudonyte, Darragh Holmes, Robert Harrison, and David Woolger are with Magnetic Shields Ltd., TN12 0DS Staplehurst, U.K.

Digital Object Identifier 10.1109/TIM.2023.3293540

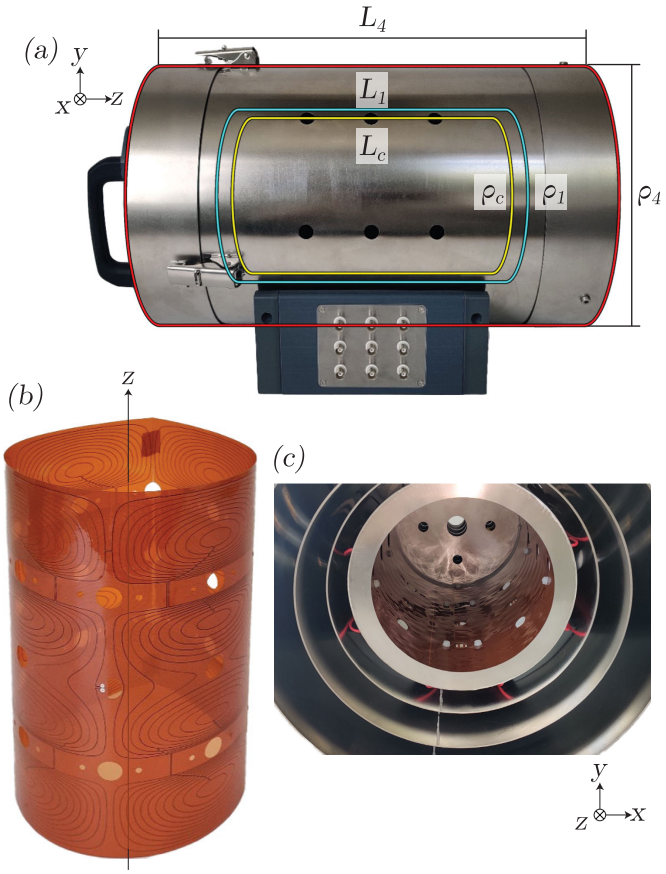

Fig. 1. Benchtop shield consists of four nested mumetal cylinders of outer radius $\rho_4 = 150$ mm and length $L_4 = 480$ mm [red] and inner radius $\rho_1 = 100$ mm and length $L_1 = 300$ mm [blue], which enclose a co-axial and co-centered set of rolled flex-PCBs of exterior radius $\rho_c = 95$ mm and length $L_c = 270$ mm [yellow]. (a) Side view of the shield and end caps, (b) rolled PCB, and (c) multiple PCBs housed inside the shield with the end cap removed.

cylinders with access holes to allow optical access and cabling (Fig. 1). Following [22] and [23], the geometries of the exterior mumetal cylinders are optimized using the NGSA-II genetic algorithm [24]. This is detailed in Appendix. The optimization returns the radii and lengths of the shield layers that maximize analytic approximations [25] for the shielding efficiency, $\mathrm{SE}_{A,T} = |\mathbf{B}^{\mathrm{unshielded}}/\mathbf{B}^{\mathrm{shielded}}|$, along and transverse to the shield's axis (A/T) while minimizing the total volume of shielding material, V, which is proportional to the shield's weight. To ensure sufficient capacity for multiple atomic magnetometers, the inner cylinder dimensions are fixed, preoptimization, to radius $\rho_1 = 100$ mm and length $L_1 = 300$ mm. The thickness of the inner mumetal layer is fixed to 0.5 mm so that the shield-induced Johnson noise, which is proportional to coil thickness [26], is reduced. The remaining shielding layers are fixed to 1.5-mm thickness to balance shielding effectiveness with total weight. Access holes are selected manually to maximize optical access to the central half inner length and diameter of the inner shield cylinder, where the flex-PCB coils generate optimized magnetic fields, without blocking the wire patterns (see Section III). The center of each end cap has a 15-mm radius access hole and is surrounded by four equally separated 7.5-mm radius access holes which are separated by 50 mm from the shield's axis. Additional holes of the same radius are placed in equally separated bands of eight at axial positions $z = [-65, 0, 65]$ mm in the cylindrical shield wall.

Next, we experimentally measure the passive shielding effectiveness of the shield by driving large uniform fields through it and measuring their attenuation inside the shield. The shield is degaussed whenever it is opened. During degaussing, a sinusoidal current with a peak-to-peak amplitude of 2 A and at a frequency of 10 Hz is driven for 10 s through four loops that are wrapped along the inner shield's axis. The amplitude of the sinusoidal current is then ramped down linearly over 60 s. The drive current is generated using a National Instruments (NI, USA) USB-6212 data acquisition module (DAQ) and is amplified using an AE Techron 7224 Power Amplifier, which is connected to a transformer to remove static offsets. The degaussing control parameters are determined by monitoring when the waveform of the induced voltage in a separate loop wrapped around the inner layer begins to distort during the fixed-amplitude phase. This provides the smallest energetic increments to remove residual magnetization during the ramping phase [27].

Sinusoidal fields of amplitude 252.5 μT are applied to the shield by driving sinusoidal current of amplitude 5 A through a 650-mm radius Ferronato[1] circular Helmholtz cage (Serviciencia S.L., Spain). The shield and Helmholtz cage are placed inside of a magnetically shielded room (MSR) to minimize background fields so that the applied field is generated predominantly by the Helmholtz cage, maximizing the signal-to-noise ratio (SNR). During all the measurements, the MSR remains closed and all the electrical sources within it are turned off, with the exception of the Helmholtz cage which is controlled remotely via cabling through a mouse hole in the MSR. The Helmholtz cage generates independent uniform fields directed along each Cartesian coordinate axis that spatially deviate by $<1\%$ from perfect uniformity in free space within a spherical volume that encompasses the entire inner shield. We use the same electronics used by the degaussing system to drive the coils, to ensure that there is no electrical noise leakage into the target uniform fields.

To determine $\mathrm{SE}_{A,T}$ at different drive frequencies, we calculate the fast Fourier transform (FFT) of the field at the center of the shield. The field is measured for 60 s using a QuSpin Zero-Field Magnetometer (QZFM) OPM and is sampled at $f_s = 200$ Hz using the standard NI LabVIEW QuSpin USB interface. The shielding efficiencies measured at the shield's center are presented in Table I. They are $\geq 10^6$ in all the cases, and the 0.2-Hz evaluations agree to within 10% of the expected results from the analytic optimization (in the static limit; see Appendix). As the applied frequency increases, the eddy currents induced in the shield increase and tend to enhance $\mathrm{SE}_{A/T}$, except for when SE_T reduces between 10 and 50 Hz. The observed behavior could potentially be explained by resonant phenomena resulting from the complex permeability of the shield, which arises from the oscillating magnetization of the ferromagnetic domains and the complex susceptibility induced by eddy currents [28]. It should be noted that the strength of

[1]Trademarked.

TABLE I

AXIAL AND TRANSVERSE SHIELDING EFFICIENCY, SE_A AND SE_T, RESPECTIVELY, AT THE CENTER OF THE BENCHTOP SHIELD SUBJECT TO A SPATIALLY UNIFORM OSCILLATORY FIELD OF FREQUENCY, f, AND PEAK-TO-PEAK AMPLITUDE $B_0 = 505\ \mu$T

f (Hz)	$SE_A \times 10^6$	$SE_T \times 10^6$
0.2	1.0 ± 0.1	20.2 ± 0.1
1	1.1 ± 0.1	23.5 ± 0.1
10	4.1 ± 0.1	39.2 ± 0.1
50	4.5 ± 0.1	19.1 ± 0.1

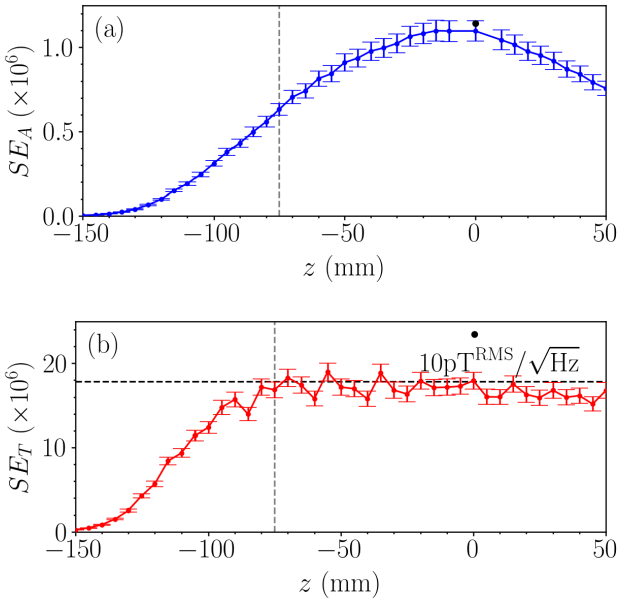

Fig. 2. (a) Axial and (b) transverse shielding efficiency, SE_A and SE_T, respectively, measured along the z-axis of the inner shield cylinder using a fluxgate magnetometer [red and blue] and an OPM [black] under $f = 1$ Hz sinusoidal drive field of peak-to-peak amplitude $B_0 = 505\ \mu$T inside an MSR. Dashed gray lines show the edge of the target field region and dashed black lines [(b) only] show the noise limit of the fluxgate magnetometer, 10 pT$^{\mathrm{rms}}\sqrt{\mathrm{Hz}}$.

the eddy currents is greater in the case of transverse shielding, given the larger shield surface area perpendicular to the applied field. However, to establish a definitive understanding of this relationship, further investigation is required.

In addition, in Fig. 2, we show $SE_{A,T}$ measured in 5-mm increments along the shield's axis measured for 1-Hz applied fields, sampled over 10 s at $f_s = 10$ kHz at each point using a Mag-13MCZ100 fluxgate magnetometer with a 24-bit Spectramag-6 DAQ (Bartington Instruments, U.K.). These measurements show good agreement with the OPM data, although the fluxgate noise floor limits the measurement of SE_T.

A representative residual magnetization profile along the shield's axis inside the MSR is measured using the fluxgate magnetometer and is shown in Fig. 3. The mean absolute field norm between $z = [-L_1/2, L_1/3]$ is (1.2 ± 0.1) nT. The static offset of the fluxgate is accounted for in these measurements by comparing the magnetic field measurements at the center of the shield with the fluxgate reading at three inverted positions, each repeated three times. As the shield has a

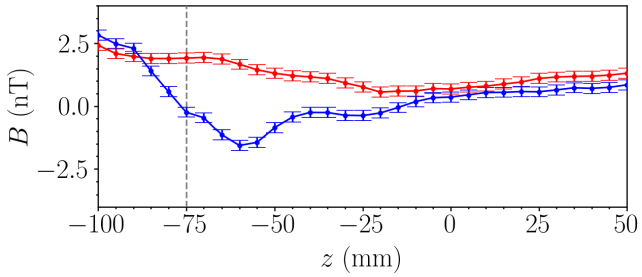

Fig. 3. Residual norm(B_x, B_y) and B_z measured along the z-axis of the inner shield cylinder using a fluxgate magnetometer [red and blue] inside an MSR. Dashed gray line shows the edge of the target field region.

high $SE_{A,T}$, the residual magnetization will dominate the field profile within the shield when compared with the transmitted field in standard conditions. However, this profile will vary between different recordings since the shield's magnetization is determined by several factors including the background that the shield has experienced, movement of the shield relative to the background, and physical impacts.

III. FLEX-PCB COILS

Next, we consider how to null static offsets using active field coils. First, we examine a streamfunction contained on the surface of a coil cylinder of radius ρ_c and length L_c, defined by

$$\varphi(\phi', z') = -\sum_{n=1}^{N'} \frac{L_c}{n\pi} W_{n0} \cos\left(\frac{n\pi\,(z' - L_c/2)}{L_c}\right) + \sum_{n=1}^{N'}\sum_{m=1}^{M'} \frac{L_c}{n\pi}\left(W_{nm}\cos(m\phi') + Q_{nm}\sin(m\phi')\right) \times \sin\left(\frac{n\pi\,(z' - L_c/2)}{L_c}\right). \quad (1)$$

The streamfunction contains modes that are weighted by Fourier coefficients (W_{n0}, W_{nm}, Q_{nm}), of order $n \in 1, \ldots, N'$ and degree $m \in 1, \ldots, M'$. As the current is confined to the surface of the cylinder, $\nabla \cdot \mathbf{J}(z', \phi') = 0$, we can express the azimuthal and axial components of the current density in terms of this basis, $J_\phi(\phi', z') = \partial\varphi(\phi', z')/\partial z'$ and $J_z(\phi', z') = -(1/\rho_c)\partial\varphi(\phi', z')/\partial\phi'$, respectively [29]. The coil patterns are generated using least-squares optimization [30], [31], [32] to find optimal values of the Fourier coefficients to generate each target field. The relationship between the magnetic field and the Fourier coefficients is encoded in [17, eqs. (37)–(39)].

Here, this method is applied to design nine flex-PCBs to generate nine low-order magnetic field harmonics within the central half length and diameter of the inner shield cylinder. We choose to generate the full set of uniform fields and linear field gradients (see Table II) and a single quadratic field gradient with respect to the axial position, d^2B_z/dz^2, to help offset the difference between SE_A and SE_T. The PCBs are co-centered and co-axial to the shield cylinder and extend over an outer radius $\rho_c = 95$ mm and length $L_c = 270$ mm.

The streamfunctions and wire patterns which generate the dB_y/dx and B_z fields are presented in Fig. 4. The uniform

TABLE II

BENCHTOP SHIELD CONTAINS NINE NESTED FLEX-PCBS WHICH GENERATE THREE ORDER $N = 1$ UNIFORM HARMONICS, FIVE $N = 2$ LINEAR HARMONICS, AND ONE $N = 3$ QUADRATIC HARMONIC, WITH SPECIFIC VARIATIONS ALONG THE CARTESIAN UNIT VECTORS, $(\hat{\mathbf{x}}, \hat{\mathbf{y}}, \hat{\mathbf{z}})$. THE MEAN FIELD STRENGTH, B_0, PER UNIT CURRENT, I, IS CALCULATED BY AVERAGING THE MEASURED FIELD ALONG $\hat{\mathbf{z}}$ BETWEEN $z = [0, L_1/4]$, EXCEPT FOR THE dB_x/dx AND dB_y/dx FIELDS WHICH ARE AVERAGED ALONG $\hat{\mathbf{x}}$ BETWEEN $x = [0, \rho_1/2]$. OVER THE SAME SPATIAL REGIONS, WE ALSO EVALUATE THE MAXIMUM DEVIATION FROM THE TARGET FIELD, $\Delta(B/r^{(N-1)}) = B/r^{(N-1)} - B_0$, AS A PERCENTAGE OF B_0

N	Target field	Target field harmonic	Coil efficiency, B_0/I (μT/(Am$^{(N-1)}$))	max $(\lvert\Delta(B/r^{(N-1)})\rvert)$ (%)
1	B_x	$B_0\hat{\mathbf{x}}$	68.9 ± 0.1	0.21 ± 0.01
	B_y	$B_0\hat{\mathbf{y}}$	68.7 ± 0.1	0.22 ± 0.01
	B_z	$B_0\hat{\mathbf{z}}$	74.2 ± 0.1	0.44 ± 0.01
2	$\mathrm{d}B_x/\mathrm{d}x$	$B_0(x\hat{\mathbf{x}} - y\hat{\mathbf{y}})$	970 ± 10	4 ± 2
	$\mathrm{d}B_y/\mathrm{d}x$	$B_0(y\hat{\mathbf{x}} + x\hat{\mathbf{y}})$	940 ± 10	4 ± 2
	$\mathrm{d}B_x/\mathrm{d}z$	$B_0(z\hat{\mathbf{x}} + x\hat{\mathbf{z}})$	430 ± 10	2 ± 1
	$\mathrm{d}B_y/\mathrm{d}z$	$B_0(z\hat{\mathbf{y}} + y\hat{\mathbf{z}})$	440 ± 10	2 ± 1
	$\mathrm{d}B_z/\mathrm{d}z$	$B_0(-x\hat{\mathbf{x}} - y\hat{\mathbf{y}} + 2z\hat{\mathbf{z}})$	1100 ± 10	1 ± 1
3	$\mathrm{d}^2B_z/\mathrm{d}z^2$	$B_0(-3xz\hat{\mathbf{x}} - 3yz\hat{\mathbf{y}} + 2z^2\hat{\mathbf{z}})$	8800 ± 100	4 ± 2

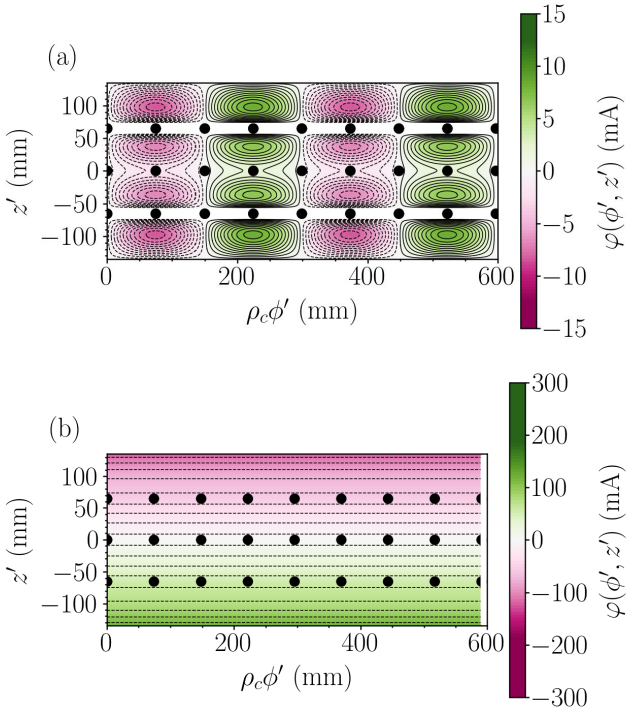

Fig. 4. Uniform (a) dB_y/dx coil design of radius $\rho_c = 94.8$ mm and (b) B_z coil design of radius $\rho_c = 92.9$ mm, which extend azimuthally over $\phi' = [0, 2\pi]$ and axially over $z' = [-L_c/2, L_c/2]$ where $L_c = 270$ mm. Black solid and dashed linestyles show opposite current flow directions; green to white to pink color shows the value of the current flow streamfunction, $\psi(\phi', z')$, from positive to zero to negative [scale right]; and black circles show access holes.

dB_y/dx coil is rolled around its azimuth to form a cylinder of radius $\rho_c = 94.8$ mm [Fig. 1(b)], whereas the uniform B_z coil is rolled into a cylinder of radius $\rho_c = 92.9$ mm. The coil patterns have different widths to allow them to be nested inside each other once rolled. The coil patterns are generated by contouring the streamfunction (1), at evenly spaced levels which span its full domain [33], [34], [35]. These patterns are selected according to which best emulates the continuum current [17] but is manufacturable, i.e., the individual wires are greater than 0.8 mm apart and do not intersect with the access holes. The PCBs are made of polyimide of 0.26-mm depth into which copper tracks comprising the wire patterns are printed and are connected together in series across two flex-PCB layers with vias. The unwanted magnetic fields generated by the connecting tracks are reduced by including tracks on the second PCB layer with opposite current flow. The current pattern which generates the uniform B_z field is composed of current loops in series, which are constructed by soldering bridges across the PCB once it is rolled. The dB_y/dx current pattern does not require solder bridges as it does not cross the edge of the PCB. The uniform B_z PCB has a track width of 1.4 mm to allow 2 A of current to be passed to produce strong axial biasing ($\sim$150 μT, without heating the shield above 40 °C from 20 °C), whereas the remaining PCBs have track widths of 0.4 mm to allow 500 mA of current. The flex-PCBs are nested inside a nylon tube and have a radial thickness of 2.5 mm in situ, including solder bridges.

The magnetic fields generated by each flex-PCB are measured by driving sinusoidal current through each PCB sequentially at a frequency of 1 Hz for 10 s and taking the FFT of the measured field. We present the profiles generated by the B_y, B_z, dB_y/dx, dB_y/dz, dB_z/dz, and d^2B_z/dz^2 PCBs in Fig. 5, evaluated along the shield's axis, except for the dB_y/dx PCB which is evaluated radially as it is designed to generate zero field along the shield's axis. The generated fields show close agreement to the target fields within the target region and rapidly deviate outside of it, thus minimizing the power consumption required to generate the desired field profile. We examine the deviation from perfect uniformity of the target fields generated by the uniform B_y and B_z PCBs in Fig. 6. The B_z profile deviates more than the B_y profile because of small error fields generated by the connections across the B_z PCB. Notwithstanding this, the fields generated by the uniform field-generating PCBs deviate from the target only by $\leq$0.5% within the target region and compare favorably to other systems optimized in similar contexts [36]. The remaining PCBs are measured to generate fields which deviate from the target by $\leq$4%; we note that intrinsic deviations are likely

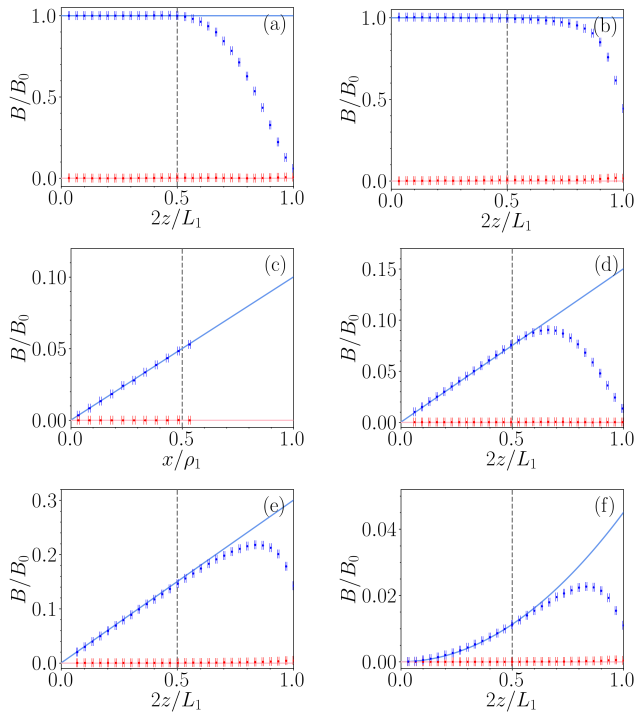

Fig. 5. Measured magnetic field in the target direction [blue] generated by the uniform (a) B_y, (b) B_z, (d) dB_y/dz, (e) dB_z/dz, and (f) d^2B_z/dz^2, flex-PCB coils plotted along the z-axis of the inner shield cylinder. In (c), the field generated by the dB_y/dx coil is plotted along the x-axis of the inner shield cylinder. The norm of the magnetic field in the other directions is measured [red] and is expected to be zero. Solid blue lines show perfect representations of the target fields and dashed gray lines show the edge of the target field region.

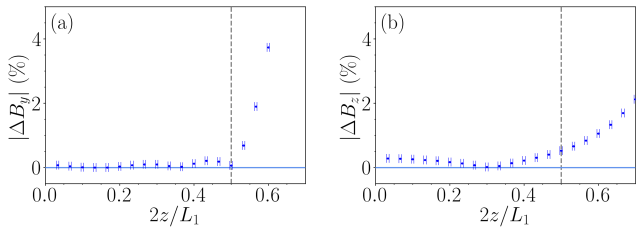

Fig. 6. Deviation between the measured and target fields for the uniform (a) B_y and (b) B_z flex-PCBs plotted versus position along the z-axis of the inner shield cylinder. Labeled as Fig. 5.

to be even smaller as gradient field measurements are highly alignment-sensitive.

IV. Active Nulling

We use a QZFM OPM to map the remnant field after degaussing at 5-mm increments along the shield's axis by calculating (B_x, B_y, B_z) values required to null the field using the onboard OPM coils using custom MATLAB code which interfaces with the OPM via NI LabVIEW. The same method as described in Section III for the fluxgate is then used to calculate the static offsets. Coil currents are calculated to null the remnant field at $N_{\text{null}} = 25$ points between $z = [-64, 56]$ mm, which extends over 40% of the inner shield length, by following the methodology outlined in [37]. Each Cartesian component of the offset-corrected magnetic field is compiled into a list of measurements, $B^{\text{mes.}}$, of length $(3N_{\text{null}})$. The coil currents required to null these fields may be related to the desired currents in each coil, I, using simple matrix algebra

$$B^{\text{ideal}}_{ji} I_i = -B^{\text{mes.}}_j \tag{2}$$

where the matrix B^{ideal} contains the expected magnetic field harmonics generated at each sampled coordinate by each flex-PCB used for nulling, assuming unitary current. Here, seven coils are used for nulling since the dB_x/dx and dB_y/dx coils generate zero field along the z-axis, and so this matrix is of dimension $(3N_{\text{null}} \times 7)$. The coil currents are obtained using (2) by calculating the pseudoinverse of B^{ideal}. The resulting coil currents, which are displayed in Table III, are at the tens of microampere level due to the low residual field within the shield. An NI-9264 voltage output module is used to generate these currents, which are then amplified using an eight-channel ±10-V amplifier constructed in-house. The amplifier is experimentally tested to have a noise level <25 nV/$\sqrt{\text{Hz}}$ at 5 Hz. To further ensure that the coil drivers do not add significant noise, each flex-PCB is driven in series with a 47-kΩ resistor.

TABLE III
Under Applied Currents, I, the Magnitudes of the Target Fields Between $z = [-64, 56]$ mm Reduce by Absolute Ratios, $|C|$

Target field	Applied current, I (μA)	Active nulling ratio, $\lvert C\rvert$
B_x	15.3	11.3
B_y	16.9	34.0
B_z	−9.4	13.1
dB_x/dz	27.4	62.4
dB_y/dz	−17.2	6.0
dB_z/dz	−3.3	9.4
d^2B_z/dz^2	−3.4	1.5

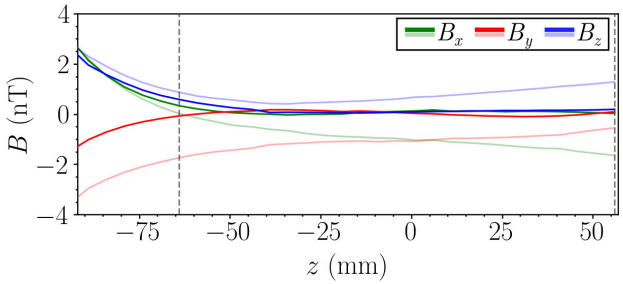

Fig. 7. B_x, B_y, and B_z [green, red, and blue; see upper right legend] along the z-axis of the inner shield cylinder with [solid] and without [light] static active background nulling between $z = [-64, 56]$ mm [gray dashed lines].

The magnetic field along the z-axis pre- and post-null and averaged over two runs is displayed in Fig. 7. The active null reduces the mean magnetic field from 1.68 to 0.23 nT. Refitting the field to the harmonic model, we calculate that the norms of the magnitudes of the three target uniform fields and four target gradients are reduced by factors of 19.5 and 19.8 after nulling, respectively (see Table III). The remaining field is dominated by contributions from higher order field harmonics at the edge of the null region. These harmonics could be alleviated by adding further target field coils to the system to null higher order gradients or using retrofitted additional coils, e.g., individually driven simple building block coils [19], for adaptive nulling of residual variations.

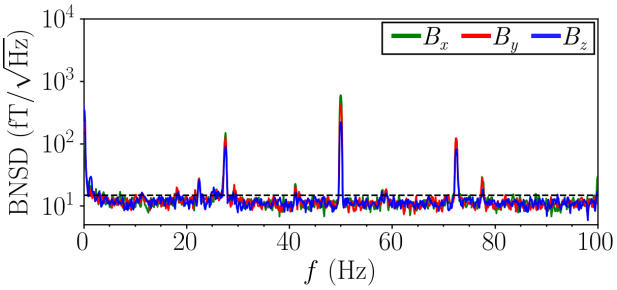

Fig. 8. Magnetic noise spectral density (BNSD) [noise limit shown by black dashed line] of the B_x, B_y, and B_z components of the magnetic field [green, red, and blue; see upper right legend]. Labeled as Fig. 7.

The magnetic noise directed along each Cartesian coordinate axis is also calculated at the shield's center by measuring the OPM output over 300 s while sampling at $f_s = 1.2$ kHz. This is displayed in Fig. 8. Generally, the noise is limited by the OPM noise floor, 15 fT/$\sqrt{\text{Hz}}$, and so the shield-induced Johnson noise is less than this value. This is consistent with the theoretically expected Johnson noise calculated from [26, eq. (16)] of ~10 fT/$\sqrt{\text{Hz}}$. The noise floor peaks at ~750 fT/$\sqrt{\text{Hz}}$ at $f = 50$ Hz due to mains electrical noise, with projections at $f = [28, 72]$ Hz due to the OPM powerline.

V. Conclusion

In this article, we have developed a magnetic field control system using optimized arrangements of mumetal magnetic shielding in conjunction with a set of nine internal flex-PCBs. The experimental measurements show that the flex-PCBs generate target magnetic fields with <4% error along the measured target regions which extend over 50% of either the inner shield diameter or length. The flex-PCBs are demonstrated to enhance the effectiveness of the passive shields. They reduce the mean static magnetic field norm to 0.23 nT over 40% of the inner shield's axis in a typical laboratory environment, which is a 7.3-fold improvement compared to the performance of the passive shields alone. Our results also demonstrate that the active coil nulling may be used without introducing significant magnetic noise. The magnitude of magnetic noise measured by a commercially available zero-field OPM was evaluated to be broadly at the sensor's 15 fT/$\sqrt{\text{Hz}}$ noise limit over much of the spectrum from 0 to 100 Hz.

The design, manufacturing, and experimental processes laid out in this work will be instructive to the development of magnetic shields in several application spaces outside of benchtop shielding. Larger shields designed using the same methods could be used similar to lightweight MSRs [38] for recording muscle [39] or gut activity [40]. Since these shields would require larger access holes, additional field-generating systems would be required to reduce leakage fields. Such coil systems may also supplement the existing shielding, enabling its partial removal, e.g., for weight reduction in spacecraft [41].

Appendix
Passive Shields Optimization

Sumner [25] generated simple approximations for the static shielding effectiveness, SE, of N_s nested layers of cylindrical passive magnetic shielding of a fixed high relative magnetic permeability, μ_r, and length greater than radius, $L_i > \rho_i$, in the flux-shunting dominated limit [42]. These are

$$\begin{aligned}\text{SE} = 1 &+ \sum_{i=1}^{N_s} \text{SE}_i + \sum_{i=1}^{N_s-1}\sum_{j>i}^{N_s} \text{SE}_i \text{SE}_j F_{ij} \\ &+ \sum_{i=1}^{N_s-2}\sum_{j>i}^{N_s-1}\sum_{k>j}^{N_s} \text{SE}_i \text{SE}_j \text{SE}_k F_{ij} F_{jk} + \cdots \\ &+ \text{SE}_{N_s} \prod_{i=1}^{N_s-1} \text{SE}_i F_{i(i+1)} \end{aligned} \tag{3}$$

where SE_i and F_{ij} are replaced by different functions depending on whether the shielding efficiency axial, SE_A, or transverse, SE_T, to the shield's axis is to be calculated. In the transverse case, they are replaced by

$$\text{SE}_{Ti} = \frac{\mu_r d_i}{2\rho_i} \tag{4}$$

$$T_{ij} = 1 - \left(\frac{\rho_i}{\rho_j}\right)^2 \tag{5}$$

whereas, in the axial case, they are replaced by

$$\text{SE}_{Ai} = 1 + \frac{\mu_r d_i}{2\rho_i}\left(\frac{K_i}{1 + \rho_i + 0.85\rho_i^2/3}\right) \tag{6}$$

$$A_{ij} = 1 - \left(\frac{L_i}{L_j}\right) \tag{7}$$

where

$$\begin{aligned} K_i = &\left(1.7 - \frac{1}{\rho_i} - 1.35\left(1 + \frac{1}{4\rho_i^3}\right)\right) \\ &\times \left(\ln\left(\rho_i + \sqrt{1+\rho_i^2}\right) - 2\left(\sqrt{1 + \frac{1}{\rho_i^2}} - \frac{1}{\rho_i}\right)\right). \end{aligned} \tag{8}$$

Here, we will use (4) and (6) with $\mu_r = 40\,000$ as objective functions for a genetic algorithm. An additional objective function is the total volume of shielding material in the cylindrical shield wall and circular end caps of the shielding layers

$$V = \sum_{i=1}^{N_s} 2\pi d_i \rho_i^2 + \pi\left(2d_i\rho_i - d_i^2\right)(L_i - 2d_i). \tag{9}$$

In the optimization system, as detailed in the main text, we fix the geometry of the inner shield cylinder and the thicknesses of all the shielding layers. The fixed values imposed in the optimization are therefore

$$\texttt{fixed vals.} \begin{cases} \rho_1 = 100 \text{ mm} \\ L_1 = 300 \text{ mm} \\ d_1 = 0.5 \text{ mm} \\ d_i = 1.5 \text{ mm}, \quad \text{for } i \in [2, 3, 4]. \end{cases} \tag{10}$$

To ensure that the shielding layers have sufficient clearance for manufacture and so the shield fits on a laboratory benchtop,

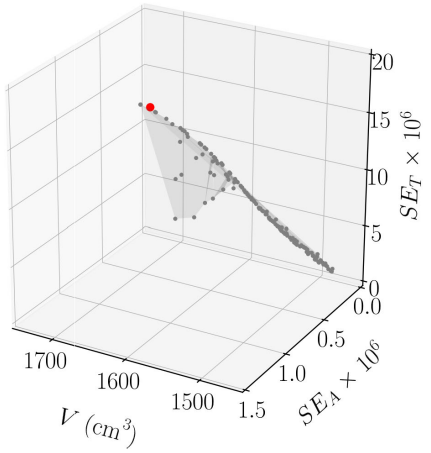

Fig. 9. Pareto front [gray scatter] where the shielding efficiencies axial, SE_A, and transverse, SE_T, to the shield's axis are maximized and the total volume of shielding material, V, is minimized. Pareto-optimal solutions are filtered to maximize SE_A [chosen solution red].

the boundaries of the search domain are constrained to

$$\texttt{search bounds}.\begin{cases}\rho_{i+1}-\rho_i>5\ \text{mm}, & \text{for } i\in[1,2,3]\\ L_{i+1}-L_i>5\ \text{mm}, & \text{for } i\in[1,2,3]\\ \rho_4\le 150\ \text{mm}\\ L_4\le 600\ \text{mm}.\end{cases} \tag{11}$$

The objectives of the optimization procedure are therefore

$$\texttt{obj}.\begin{cases}\max \mathrm{SE}_T(\rho_2,\rho_3,\rho_4,L_2,L_3,L_4)\\ \max \mathrm{SE}_A(\rho_2,\rho_3,\rho_4,L_2,L_3,L_4)\\ \min V(\rho_2,\rho_3,\rho_4,L_2,L_3,L_4).\end{cases} \tag{12}$$

The NSGA-II genetic algorithm is used to find solutions for the objective functions laid out in (12), subject to the search domain constraints outlined in (11). The NGSA-II control parameters used match those in [19], except that the population size is set to 250. Convergence is achieved after 112 generations of the algorithm, requiring 28 000 evaluations of each objective function. This takes 42.6 s on a MacBook Pro16,1 which is equipped with a 6-Core Intel Core i7 2.6-GHz processor and 16 GB of DDR4 RAM. The output Pareto front is presented in Fig. 9. The solution with the highest axial shielding efficiency is selected, where the axial and transverse shielding efficiencies are $\mathrm{SE}_A = 1.1\times10^6$ and $\mathrm{SE}_T = 19\times10^7$, respectively, for fixed $\mu_r = 40\,000$. These values deviate from the lowest frequency (0.2 Hz) experimentally measured values in Table I by 10%, although are highly sensitive to the value of initial relative permeability selected in the optimization. Thus, discrepancies are anticipated as the analytic formulae are approximations in the static limit and assume fixed permeability of each layer. Conversely, in the experimental measurements, the inner layers of mumetal will experience a reduced field magnitude, changing their effective permeability [43].

Declarations

Peter J. Hobson, Michael Packer, Dominic Sims, Matthew J. Brookes, Richard Bowtell, and Mark Fromhold have a worldwide patent (WO/2021/053356) which includes the coil design technique applied in this work. Ben Styles, Prashant Patel, James Chalmers, and David Woolger are employees of Magnetic Shields Ltd., U.K., who sell benchtop shields commercially. Sintija Raudonyte, Darragh Holmes, and Robert Harrison are ex-employees of MSL. Niall Holmes, David Woolger, Matthew J. Brookes, and Richard Bowtell hold founding equity in Cerca Magnetics Ltd., U.K., who commercialize OPM technology. Chris Morley, Alister Davis, and Thomas X. Smith declare no competing interests.

Magnetic Shields Limited have made the benchtop shield available for purchase (see [44]).

This work has been submitted to the IEEE for possible publication. Copyright may be transferred without notice, after which this version may no longer be accessible.

All supporting data may be made available on request.

References

[1] J. Xu, Q. You, Z. Li, B. Han, Z. Zhang, and Q. He, "The elimination of the effect of the external field in the Joule balance," *IEEE Trans. Instrum. Meas.*, vol. 69, no. 4, pp. 1745–1752, Apr. 2020.

[2] S. Afach et al., "Dynamic stabilization of the magnetic field surrounding the neutron electric dipole moment spectrometer at the Paul Scherrer institute," *J. Appl. Phys.*, vol. 116, no. 8, Aug. 2014, Art. no. 084510.

[3] F. M. Stürner et al., "Integrated and portable magnetometer based on nitrogen-vacancy ensembles in diamond," *Adv. Quantum Technol.*, vol. 4, no. 4, Apr. 2021, Art. no. 2000111.

[4] F. Bertrand et al., "A 4He vector zero-field optically pumped magnetometer operated in the earth-field," *Rev. Sci. Instrum.*, vol. 92, no. 10, Oct. 2021, Art. no. 105005.

[5] S. P. Krzyzewski, A. R. Perry, V. Gerginov, and S. Knappe, "Characterization of noise sources in a microfabricated single-beam zero-field optically-pumped magnetometer," *J. Appl. Phys.*, vol. 126, no. 4, Jul. 2019, Art. no. 044504.

[6] P. Bevington, R. Gartman, W. Chalupczak, C. Deans, L. Marmugi, and F. Renzoni, "Non-destructive structural imaging of steelwork with atomic magnetometers," *Appl. Phys. Lett.*, vol. 113, no. 6, Aug. 2018, Art. no. 063503.

[7] I. Kominis, T. Kornack, J. Allred, and M. Romalis, "A subfemtotesla multichannel atomic magnetometer," *Nature*, vol. 422, pp. 596–599, May 2003.

[8] V. K. Shah and R. T. Wakai, "A compact, high performance atomic magnetometer for biomedical applications," *Phys. Med. Biol.*, vol. 58, no. 22, pp. 8153–8161, Nov. 2013.

[9] R. M. Hill et al., "Using OPM-MEG in contrasting magnetic environments," *NeuroImage*, vol. 253, Jun. 2022, Art. no. 119084.

[10] E. Boto et al., "Triaxial detection of the neuromagnetic field using optically-pumped magnetometry: Feasibility and application in children," *NeuroImage*, vol. 252, May 2022, Art. no. 119027.

[11] Y. Hu et al., "Rapid online solid-state battery diagnostics with optically pumped magnetometers," *Appl. Sci.*, vol. 10, no. 21, p. 7864, Nov. 2020.

[12] Y. Hu et al., "Sensitive magnetometry reveals inhomogeneities in charge storage and weak transient internal currents in Li-ion cells," *Proc. Nat. Acad. Sci. USA*, vol. 117, no. 20, pp. 10667–10672, May 2020.

[13] A. Borna et al., "Cross-axis projection error in optically pumped magnetometers and its implication for magnetoencephalography systems," *NeuroImage*, vol. 247, Feb. 2022, Art. no. 118818.

[14] Y. Fu, Z. Wang, L. Xing, W. Fan, J. Ruan, and H. Pang, "Suppression of nonuniform magnetic fields in magnetic shielding system for SERF co-magnetometer," *IEEE Trans. Instrum. Meas.*, vol. 71, pp. 1–8, 2022.

[15] I. Altarev et al., "Minimizing magnetic fields for precision experiments," *J. Appl. Phys.*, vol. 117, no. 23, Jun. 2015, Art. no. 233903.

[16] Z. Sun, M. Reisner, P. Fierlinger, A. Schnabel, S. Stuiber, and L. Li, "Dynamic modeling of the behavior of permalloy for magnetic shielding," *J. Appl. Phys.*, vol. 119, no. 19, May 2016, Art. no. 193902.

[17] M. Packer et al., "Optimal inverse design of magnetic field profiles in a magnetically shielded cylinder," *Phys. Rev. Appl.*, vol. 14, no. 5, Nov. 2020, Art. no. 054004.

[18] M. Packer et al., "Planar coil optimization in a magnetically shielded cylinder," *Phys. Rev. Appl.*, vol. 15, no. 6, Jun. 2021, Art. no. 064006.

[19] M. Packer et al., "Magnetic field design in a cylindrical high-permeability shield: The combination of simple building blocks and a genetic algorithm," *J. Appl. Phys.*, vol. 131, no. 9, Mar. 2022, Art. no. 093902.

[20] F. Zhao, X. Zhou, W. Zhou, X. Zhang, K. Wang, and W. Wang, "Research on the design of axial uniform coils for residual field compensation in magnetically shielded cylinder," *IEEE Trans. Instrum. Meas.*, vol. 71, pp. 1–9, 2022.

[21] H. Pang et al., "Design of highly uniform field coils based on the magnetic field coupling model and improved PSO algorithm in atomic sensors," *IEEE Trans. Instrum. Meas.*, vol. 71, pp. 1–11, 2022.

[22] P. J. Hobson et al., "Optimised hybrid shielding and magnetic field control for emerging quantum technologies," *Proc. SPIE*, vol. 11881, pp. 111–120, Mar. 2021.

[23] J. Li, Z. Wang, and W. Quan, "Multi-objective optimization of multilayer passive magnetic shield based on genetic algorithm," *AIP Adv.*, vol. 9, no. 12, Dec. 2019, Art. no. 125210.

[24] K. Deb, A. Pratap, S. Agarwal, and T. Meyarivan, "A fast and elitist multiobjective genetic algorithm: NSGA-II," *IEEE Trans. Evol. Comput.*, vol. 6, no. 2, pp. 182–197, Apr. 2002.

[25] T. J. Sumner, J. M. Pendlebury, and K. F. Smith, "Convectional magnetic shielding," *J. Phys. D, Appl. Phys.*, vol. 20, no. 9, pp. 1095–1101, Sep. 1987.

[26] S.-K. Lee and M. V. Romalis, "Calculation of magnetic field noise from high-permeability magnetic shields and conducting objects with simple geometry," *J. Appl. Phys.*, vol. 103, no. 8, Apr. 2008, Art. no. 084904.

[27] F. Thiel, A. Schnabel, S. Knappe-Grüneberg, D. Stollfuß, and M. Burghoff, "Demagnetization of magnetically shielded rooms," *Rev. Sci. Instrum.*, vol. 78, no. 3, Mar. 2007, Art. no. 035106.

[28] D.-X. Chen and C. Gu, "AC susceptibilities of conducting cylinders and their applications in electromagnetic measurements," *IEEE Trans. Magn.*, vol. 41, no. 9, pp. 2436–2446, Sep. 2005.

[29] J. D. Jackson, *Classical Electrodynamics*, 3rd ed. New York, NY, USA: Wiley, 1999.

[30] P. T. Boggs and J. W. Tolle, "Sequential quadratic programming," *Acta Numer.*, vol. 4, pp. 1–51, Jan. 1995.

[31] C. A. Floudas and V. Visweswaran, "Quadratic optimization," in *Handbook of Global Optimization*. Cham, Switzerland: Springer, 1995, pp. 217–269.

[32] J. W. Carlson, K. A. Derby, K. C. Hawryszko, and M. Weideman, "Design and evaluation of shielded gradient coils," *Magn. Reson. Med.*, vol. 26, no. 2, pp. 191–206, Aug. 1992.

[33] L. K. Forbes and S. Crozier, "A novel target-field method for finite-length magnetic resonance shim coils: I. Zonal shims," *J. Phys. D, Appl. Phys.*, vol. 34, no. 24, pp. 3447–3455, Dec. 2001.

[34] L. K. Forbes and S. Crozier, "A novel target-field method for finite-length magnetic resonance shim coils: II. Tesseral shims," *J. Phys. D, Appl. Phys.*, vol. 35, no. 9, pp. 839–849, May 2002.

[35] L. K. Forbes and S. Crozier, "A novel target-field method for magnetic resonance shim coils: III. Shielded zonal and tesseral coils," *J. Phys. D, Appl. Phys.*, vol. 36, no. 2, pp. 68–80, Jan. 2003.

[36] P. J. Hobson et al., "Bespoke magnetic field design for a magnetically shielded cold atom interferometer," *Sci. Rep.*, vol. 12, no. 1, pp. 1–12, Jun. 2022.

[37] M. Rea et al., "Precision magnetic field modelling and control for wearable magnetoencephalography," *NeuroImage*, vol. 241, Nov. 2021, Art. no. 118401.

[38] N. Holmes et al., "A lightweight magnetically shielded room with active shielding," *Sci. Rep.*, vol. 12, no. 1, p. 8, Aug. 2022.

[39] P. J. Broser, T. Middelmann, D. Sometti, and C. Braun, "Optically pumped magnetometers disclose magnetic field components of the muscular action potential," *J. Electromyogr. Kinesiol.*, vol. 56, Feb. 2021, Art. no. 102490.

[40] C. E. Eichler, L. K. Cheng, N. Paskaranandavadivel, P. Du, L. A. Bradshaw, and R. Avci, "Effects of magnetogastrography sensor configurations in tracking slow wave propagation," *Comput. Biol. Med.*, vol. 129, Feb. 2021, Art. no. 104169.

[41] A. Junge and F. Marliani, "Prediction of DC magnetic fields for magnetic cleanliness on spacecraft," in *Proc. IEEE Int. Symp. Electromagn. Compat.*, Aug. 2011, pp. 834–839.

[42] R. A. S. Celozzi and G. Lovat, *Appendix B: Magnetic Shielding*. Hoboken, NJ, USA: Wiley, 2008.

[43] T. Andalib et al., "Sensitivity of fields generated within magnetically shielded volumes to changes in magnetic permeability," *Nucl. Instrum. Methods Phys. Res. A, Accel. Spectrom. Detect. Assoc. Equip.*, vol. 867, pp. 139–147, Sep. 2017.

[44] Magnetic Shields Limited. *GA4 Hybrid Shield*. [Online]. Available: http://www.magneticshields.co.uk/product-mumetal-shields

Peter J. Hobson received the M.Phys. degree in theoretical physics from Durham University, Durham, U.K., in 2018, the M.Res. degree in translational quantum technology from the University of Birmingham, Birmingham, U.K., in 2020, and the Ph.D. degree from the University of Nottingham, Nottingham U.K., in 2022, where his thesis was titled "Magnetic Field Design for Quantum Technologies."

He is currently an EPSRC, Swindon, U.K., Doctoral Prize Fellow with the University of Nottingham. His research interests include magnetic field design, optimizing electromagnetic shielding, and next-generation quantum sensors.

Niall Holmes received the M.Sci. and Ph.D. degrees in physics from the University of Nottingham, Nottingham, U.K., in 2016 and 2020, respectively.

He is currently a Research Fellow with the Sir Peter Mansfield Imaging Centre, University of Nottingham, developing active magnetic field control for biomagnetic measurements, particularly wearable magnetoencephalography.

Prashant Patel received the M.Phys. degree in physics from the University of Leicester, Leicester, U.K., in 2019.

In 2020, he joined the Research and Development Team at Magnetic Shields Ltd., Staplehurst, U.K. He is the Technical Lead on projects understanding the capabilities of magnetic shielding materials, using his expertise in electromagnetism and soft magnetic materials.

Ben Styles received the B.Eng. degree (Hons.) in electronic and electrical engineering from the University of Brighton, Brighton, U.K., in 2020.

He is currently a Senior Electronics Engineer with Magnetic Shields Ltd., Staplehurst, U.K. His expertise lies mainly in PCB design and analog electronics. He is also working on compact coil arrays, made of either flexible PCBs or complex 3-D geometrics, as well as developing low-noise electronic designs to drive those coils and related systems.

James Chalmers received the M.Phys. degree in physics with astrophysics from the University of Kent, Canterbury, U.K., in 2018.

In 2019, he joined at Magnetic Shields Ltd., Staplehurst, U.K., as a Physicist. He was promoted to a Research and Development Manager in 2021. His team focuses on the development of active shielding and degaussing technologies for use in magnetically shielded rooms and other shielding products that require ultralow fields.

Chris Morley received the M.Sci. and Ph.D. degrees in physics from the University of Nottingham, Nottingham, U.K., in 2016 and 2020, respectively. He successfully defended his thesis, "Optimization and Simulation of Magneto Optical Traps for Quantum Technologies."

He is currently a Post-Doctoral Researcher with the University of Nottingham, where his work focuses on magnetic field design and simulations to enable emerging quantum technologies.

Alister Davis received the M.Phys. degree (Hons.) in physics from the University of Nottingham, Nottingham, U.K., in 2019. He is currently pursuing the Ph.D. degree in theoretical physics with the University of Nottingham, where his research focuses on magnetic shielding for quantum experiments. He has a particular interest in the manufacturing of complex coil designs and is expected to complete his Ph.D. in 2023.

Michael Packer received the M.Sci. degree in theoretical physics from the University of Birmingham, Birmingham, U.K., in 2016, and the Ph.D. degree in physics from the University of Nottingham, Nottingham, U.K., in 2021.

He was a Post-Doctoral Researcher at the University of Nottingham focused on the optimization of interacting electromagnetic systems, before transitioning into quantitative financial research.

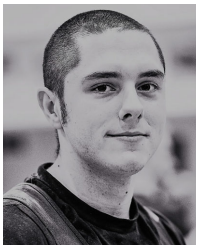

Thomas X. Smith received the M.Phys. degree in physics from the University of Nottingham, Nottingham, U.K., in 2022. He is currently pursuing the Ph.D. degree in physics, with a focus on the design and creation of additively manufactured magnetic shields.

Sintija Raudonyte received the M.Sci. degree in physics from Imperial College London, London, U.K., in 2021.

She has experience in experimental research of magnetic shield design and software engineering (experiment automation, data analysis, and app development). She is currently a Software Engineer with Samphire Neuroscience, London, U.K., developing a wearable neuromodulation device using transcranial direct current stimulation to treat depression and pain caused by premenstrual dysphoric disorder and related conditions.

Darragh Holmes received the B.Eng. degree in engineering from the Trinity College Dublin, Dublin, Ireland, in 2009.

Until 2022, he was an Engineering Manager with Magnetic Shields Ltd., Staplehurst, U.K., designing shielding systems for satellites, fundamental physics, and noninvasive cardiac and neural imaging.

Robert Harrison received the M.Eng. degree in mechanical engineering with mechatronics from the University of Southampton, Southampton, U.K., in 2019.

From 2020 to 2021, he worked at Magnetic Shields Ltd., Staplehurst, U.K., where he specialized in the mechanical design of enclosures to provide an area of low magnetic field.

David Woolger joined at Magnetic Shields Ltd., Staplehurst, U.K., as a Commercial Director in 2012 before taking on the role of the Managing Director in 2014. He has led the global expansion of the business and has been responsible for driving forward research and development, innovation, and design within the magnetic field design industry. He became the CEO of Cerca Magnetics Ltd., Nottingham, U.K., who are developing brain scanners using optically pumped magnetometers, in 2020.

Dominic Sims received the B.Eng. degree in aeronautical engineering from the Royal Melbourne Institute of Technology, Melbourne, Australia, in 1990, and the Master of Business Administration degree from the Australian Graduate School of Management, University of New South Wales, Sydney, Australia, in 2010.

He has been the Business Development Manager for Quantum Technologies with the University of Nottingham, Nottingham, U.K., since 2015.

Matthew J. Brookes received the Ph.D. degree from the University of Nottingham, Nottingham, U.K., in 2005.

He is currently a Professor of physics with the University of Nottingham. His research interests include development and application of multimodal functional brain imaging and brain imaging modality called magnetoencephalography. These techniques have significant impact on multiple clinical fields, including examining traumatic head injuries and diagnosing schizophrenia and epilepsy.

Richard Bowtell received the B.A. degree in natural sciences from Cambridge University, Cambridge, U.K., in 1984, and the Ph.D. degree in physics from the University of Nottingham, Nottingham, U.K., in 1988.

He has spent his career with the School of Physics and Astronomy, Nottingham, having been appointed to a lectureship in 1989 and the Chair in 2000. He served as the Head of School of Physics and Astronomy, from 2008 to 2014, where he is currently the Director of the Sir Peter Mansfield Imaging Centre, Nottingham. His research interests span magnetic resonance imaging and spectroscopy and magnetoencephalography and include the design of magnetic field control systems for both the modalities.

Mark Fromhold received the B.Sc. degree (Hons.) in physics from Durham University, Durham, U.K., in 1986, and the Ph.D. degree in theory of quantum tunneling in semiconductor heterostructures from the University of Nottingham, Nottingham, U.K., in 1990.

After Post-Doctoral Research at the University of Warwick, Coventry, U.K., and an EPSRC U.K. Advanced Research Fellowship, in 2000, he re-joined the University of Nottingham. Since August 2020, he has been the Head of the School of Physics and Astronomy, Nottingham. His present research interests include development and integration of electronic, cold-atom, and electromagnetic systems as components for quantum technologies.